# Chapter-4

# Pyrolysis behavior of low value biomass (*Lagerstroemia speciosa* seed hull): Evaluation of kinetic, thermodynamics, and product characterization

## 4.1 Introduction

In today's world, biomass and biofuels are increasing popularity owing to their abundant availability, low or insignificant cost, clean and sustainable nature. Aside from that, biomass offers several additional advantages, such as lower sulfur and nitrogen content, which results in fewer SOx and NOx emissions, and employment for those who source the biomass. In the present work, thermal degradation of *Lagerstroemia speciosa* seed hull (LS) was carried out. *Lagerstroemia speciosa* is a *Lagerstroemia* species native to southern tropical Asia. It is a fast-growing, medium-sized tree mostly found in India, Myanmar, Philippines, Cambodia, Singapore, Thailand, Vietnam, etc. It is commonly grown in lawns, yards, parking sides, parks, and highways for decorative purposes. The quality of the wood is excellent, and often traded as one of the best timber trees in Assam (India) and Myanmar. It usually flowers in summer in India, and the plants shed their seeds in winter [88]. *Lagerstroemia speciosa* is a large tree with many stems that deviate from above ground level. The shape of the fruit is like the wooded shell on a firm calyx. After pollination, the total seed production per tree is about 932.15±63.37 kg; the potential for regeneration is minimal and cultivated, propagated by pruning and rooting [89].

For designing a pyrolysis reactor, it is necessary to achieve a good understanding of the kinetic as well as thermodynamic parameters [90]. Thermogravimetric analysis (TGA) is a frequently used technique to understand the thermal degradation kinetic parameters and the prevailing reaction mechanism, utilizing only a small amount of the sample [56]. Thermochemical, biochemical, and mechanical extraction are techniques for converting biomass into usable commodities. The thermochemical conversion process includes combustion, liquefaction, and pyrolysis. Pyrolysis has received far more attention in recent years than any other sort of thermochemical process, owing to its inherent advantages. Pyrolysis is the thermal breakdown of biomass in the absence of oxygen, in which the biomass is burned to create carbonaceous

char, oil, and flammable gases [91]. The yield of pyrolysis products is determined by a number of factors, for example, type of biomass, catalyst employed, heating rate, size of the feedstock, sweeping gas ($N_2$) flow rate, reactor layout, and temperature [92,93]. Among these, temperature, inert gas ($N_2$) flow rate, and heating rate significantly influences the pyrolysis product output. For pyrolysis, optimizing these parameters is necessary to get the reactor's high efficiency, design, and economy. Researchers generally used OFAT (one factor at a time) method to optimize the process parameters. In this method, one factor varies, and the others remain constant. However, it is time-consuming and not feasible for complex processes such as pyrolysis [79]. As a result, the limitations of such traditional approaches may be avoided by optimizing the process parameters using statistical experimental design through response surface methodology (RSM).

The present work was carried out with the aim of investigating the thermochemical characteristics and thermal degradation behavior of LS biomass. The measured residual weight-temperature data at different heating rates were used to evaluate the kinetic and thermodynamic parameters of the pyrolysis process with the help of isoconversional methods. The underlying reaction mechanism was elucidated using the $z(\alpha)$ master plot. In addition, the RSM technique based on central composite design (CCD) was used to optimize the important operating variables like heating rate, $N_2$ gas flow rate, and temperature for obtaining the maximum amount of bio-oil. The obtained liquid product was characterized via FTIR, GCMS, and 1H-NMR, whereas the biochar was characterized based on their physicochemical characteristics.

### 4.2 Physicochemical characteristics of LS biomass

The physicochemical characterization of biomass was carried out by using proximate and ultimate analysis as per ASTM protocol (ASTM E871, ASTM E1755, and ASTM E872); however, C, H, N, and S (elemental analysis) were determined using an elemental analyzer

(Euro, EA 3000 Italy). In addition, the sample's calorific value (HHV) was computed by an oxygen bomb calorimeter (Rajdhani Scientific Instrument Company, New Delhi, India). Finally, the fiber analysis of biomass (cellulose, hemicellulose, and lignin) was estimated as per the method defined in section 3.2.7. The different functional groups in the LS biomass were identified using Fourier Transform Infrared Spectroscopy (FTIR, Model: FTS 3500 GX). The dried KBr powder was evenly mixed with the sample at a ratio of 1:100 and inserted into the sample container. Scanning was performed at 40 with a step size of 4 $cm^{-1}$ within a 400 – 4000 $cm^{-1}$ wavelength range.

### 4.3 Thermal analysis

A thermogravimetric analyzer (Shimadzu Asia Pacific Pvt. Ltd, Singapore) was employed for the thermal degradation behavior of the LS biomass to understand the mass loss pattern against the time or temperature in the temperature range of 30 – 700 °C and heating rate of 10 °C/min with a steady flow of nitrogen (100 ml/min) throughout the experiment. Furthermore, the sample was pyrolyzed in the same TGA at dynamic heating rates of 10, 15, 20, 30, and 40 °C/min. The experiment was repeated thrice for the accuracy of data, and the acquired data from the TGA was utilized for further investigation.

### 4.4 Design of experiment using RSM

The yield and qualities of the pyrolysis product are closely related to process factors. The heating rate, temperature, and $N_2$ flow rate are all critical elements in determining the pyrolysis product yield. As a result, optimizing these process factors prior to testing becomes crucial. The current study is centered on optimizing important pyrolysis characteristics likewise temperature, heating rate, and inert gas ($N_2$) flow rate as independent variables, while bio-oil yield was chosen as a dependent variable using design expert (DE) software (Statease USA, 11) based on central composite design (CCD). This method is widely used since it involves only a few operations to optimize the response variable and provides an easy way to examine

the interactions between numerous parameters. A series of 20 trials were carried out in accordance with the design expert software, consisting of 6, 8, and 6 axial, factorial, and center points, respectively, with duplicates at five different levels (-alpha, +alpha, -1, +1, 0), as shown in Eq. (4.1) below.

$$N = 2^n + 2n + n_c = 2^3 + 2 \times 3 + 6 = 20 \quad (4.1)$$

where N signifies the total number of trials to be performed, n is the number of independent variables, and $n_c$ is the number of repeats at center locations. A 2nd-degree model equation was used to fit all of the experimental findings.

$$Y = \beta_o + \sum_{i=1}^{n} \beta_i X_i + \sum_{i=1}^{n} \beta_{ii} X_i^2 + \sum_{i=1}^{n} \sum_{j>1}^{n} \beta_{ij} X_i X_j \quad (4.2)$$

where Y stands for the predicted response, n stands for total experimental runs, and $\beta_o, \beta_i, \beta_{ii}, and\ \beta_{ij}$ stand for constant, linear, quadratic, and interaction term regression coefficients, respectively. Furthermore, the fitness of the regression model was tested using ANOVA and regression analysis at a 95% confidence level using Design Expert software.

### 4.5 Physicochemical characterization of pyrolysis products

A graduated cylinder and weighing machine were used to calculate the bulk density, while a Brookfield viscometer was employed to calculate the viscosity of bio-oil at 30°C and 50 rpm. The acidity of the biochar and liquid was determined by employing a pH meter (CL-54, TI, Ajmer). The Shimadzu QP-2010 plus apparatus was employed to perform GCMS (gas chromatography-mass spectrometry) investigation to recognize various chemical components contained in the bio-oil. The GCMS instrument was equipped with a Rxi-5ms column. The sample injection volume was kept constant at 1µl for the GCMS analysis, with a split ratio of 10. The carrier gas employed here is helium with a regulated flow rate of 1 ml/min. The GC oven was preheated to 50°C/min for 10 min before being raised to 150°C/min at a rate of

4°C/min. This temperature was maintained for 2 minutes before reaching a temperature of 280 °C by increasing at the rate of 10 °C/min and keeping it for 30 min. The chemical constituents were analyzed by comparing their mass spectra to those with the NIST library database. Bruker Advance (500 MHz, Biospin Canada) spectrometer was employed for 1H-NMR spectra of the bio-oil. The bio-oil was filtered using a 0.22µm filter disk and mixed with $CDCl_3$ (0.6 ml). The surface morphology of biochar was examined through a field emission scanning electron microscope (FE-SEM, Nova Nano SEM 450) and an energy dispersive X-ray (EDX).

## 4.6 Results and discussion

### 4.6.1 Characteristics

Table 4.1 listed the physicochemical analysis of LS biomass and compared it with some other reported biomass (pine sawdust, sal sawdust, and areca nut husk) [7]. The comparison of biomass presented in Table 4.1 disclosed that the volatile matter of LS (74.10%) is equivalent to areca nut husk (74.05%); however, it is less than pine sawdust (78.03%) and sal sawdust (76.03%), which underscores the higher ignition rate of the biomass. Moreover, the biomass associated with higher volatile matter, especially organic content, favored the formation of a higher volume of liquid fuel. The ash content was 2.60 %, which agrees with the testified biomass [7]. The moisture level of the LS biomass is found to be 3.7%. Earlier studies suggested that biomass containing less than 10% moisture content is a more promising feedstock for pyrolysis [94,95]. Further, the fixed carbon amount was found to be 19.6% which matches well with other testified biomass as listed in Table 4.1, a pointer to the higher energy value of the LS. The ultimate study of LS discloses a slightly lower carbon content (38.94%) than the compared study of other testified biomass. However, the nitrogen content of LS biomass was found to be slightly higher (1.02%) than the value reported for other testified biomass. The varied elemental composition of biomass was ascribed to the difference in composition of biomass [81]. The HHV (higher heating value) of LS was 17.57 MJ/kg is

comparable to pine sawdust, areca nut husk, and sal sawdust. The HHV of the biomass was an outcome of the elemental composition of biomass; thus, when the composition of biomass changed, the HHV of biomass varied substantially. The bulk density of LS biomass was found to be 478.12 kg/$m^3$. The higher bulk density of biomass presaged easy transportation and storage. The fiber analysis of LS biomass revealed 51.33 wt. % cellulose, 26.69 wt. % hemicelluloses, and 21.95 wt. % lignin, which agrees well with the published research of Mishra et al., [7].

### 4.6.2 Van-Krevelen plot

The Van-Krevelen diagram was used to demonstrate the energy content of LS on a molar ratio basis, which was compared well with other testified biomass [7,59,96–98] and is displayed in Fig. 4.1. It can be seen from Fig. 4.1 that LS biomass has greater molar ratios than coal and exhibited comparable value with other testified biomass. Notably, O/C and H/C ratios of biomass depend on the type, composition, and geographical locations where they have been grown. The molar ratios are directly connected to the biomass energy content that depends on the bonds (O-C and H-C) found within the sample. Furthermore, biomass having lower molar ratios values verified its energy and placed it near coal. The slight variations in the O/C and H/C ratios of all the chosen biomass were attributed to chemical components, biomass kinds, environmental circumstances, etc.

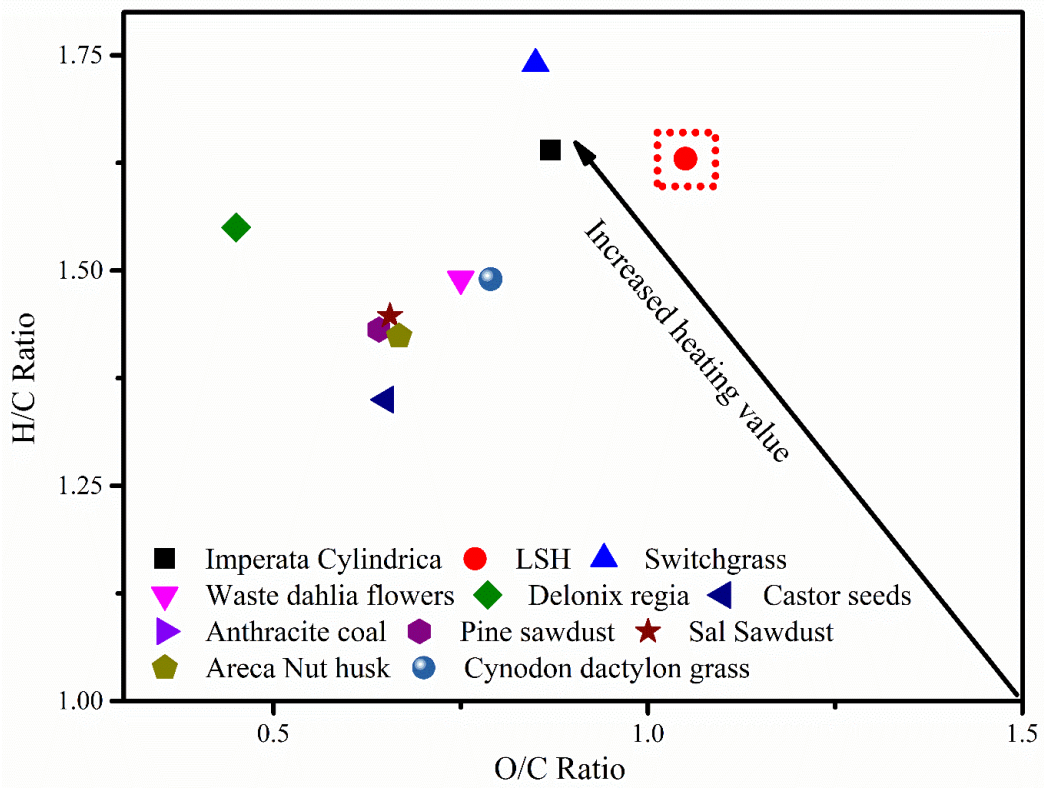


**Fig. 4.1:** Van-Krevelen diagram for different biomass and coals

**Table 4.1:** Physicochemical study of the LS biomass along with some other reported biomass

| Parameter | LS | Pine sawdust [7] | Sal sawdust [7] | Areca nut husk [7] |
|---|---|---|---|---|
| Proximate analysis (wt. %) | | | | |
| Moisture[a] | 3.7±0.10 | 6.09±0.3 | 8.88±0.2 | 7.43±0.1 |
| Volatile matter[b] | 74.10±0.40 | 78.03±0.2 | 76.03±0.1 | 74.05±0.2 |
| Ash content[b] | 2.60±0.20 | 2.07±0.03 | 1.14±0.01 | 2.48±0.05 |
| Fixed carbon[b,c] | 19.60±0.60 | 12.16±0.1 | 14.09±0.2 | 15.55±0.3 |
| Ultimate analysis (%) | | | | |
| Carbon[b] | 38.94±0.20 | 50.30 | 49.83 | 48.80 |
| Hydrogen[b] | 5.34±0.05 | 6.00 | 6.01 | 5.79 |
| Oxygen[b,c] | 54.45±0.80 | 42.99 | 43.56 | 43.45 |
| Nitrogen[b] | 1.02±0.04 | 0.69 | 0.58 | 1.95 |
| Sulfur[b] | 0.25±0.01 | - | - | 0.1 |

| | | | | |
|---|---|---|---|---|
| H/C ratio | 1.63 | 1.42 | 1.43 | 1.41 |
| O/C ratio | 1.05 | 0.64 | 0.65 | 0.67 |
| HHV (MJ/kg) | 17.57±1.1 | 18.44 ± 09 | 18.20 ± 09 | 18.21 ± 09 |
| Bulk density[a] ($Kg/m^3$) | 478.12±1.6 | 296.27 ± 16 | 321.91± 20 | 248.56 ± 11 |
| Fiber analysis (wt. %) | | | | |
| Cellulose[b] | 51.35±0.80 | 55.92 | 52.36 | 48.98 |
| Hemicellulose[b] | 26.69±0.10 | 15.35 | 14.59 | 16.81 |
| Lignin[b] | 21.95±1.20 | 10.55 | 11.18 | 13.27 |

[a] Wet basis; [b] Dry basis; [c] By difference

### 4.6.3 FTIR analysis of biomass

The study of the functional groups of LS biomass is essential to access useful functional groups present in the biomass. The functionality of the LS biomass was estimated using an FTIR analyzer and subsequently plotting a graph between wavenumber and transmittance; the data thus generated is displayed in Fig. 4.2. Peak at 3310 $cm^{-1}$ established attendance of chemically bound hydroxyl group (–OH) that mainly indicates the occupancy of alcohol, phenol, acid, water, and proteins [99,100]. Furthermore, the band peak 2915 $cm^{-1}$ was assigned to the asymmetric and symmetric vibrations (alkanes) of C-$H_2$ and C-$H_3$. [99,100]. The 1375 $cm^{-1}$ band peak represented the occurrence of methyl-and phenolic groups of C-H and aliphatic C-$H_2$ [100]. Further, the 1620 $cm^{-1}$ band peak assigned to the C=C aromatic ring showed the presence of the lignin-rich groups and proteins in the sample. Moreover, cellulose, hemicellulose, and lignin were found in the band's peak at 1021 $cm^{-1}$ allocations for C-O stretching vibration [99]. The adsorption band confirmed the existence of mono and polycyclic substituted aromatics groups at 799 $cm^{-1}$, which was qualified for O-H bending vibrations. [61].

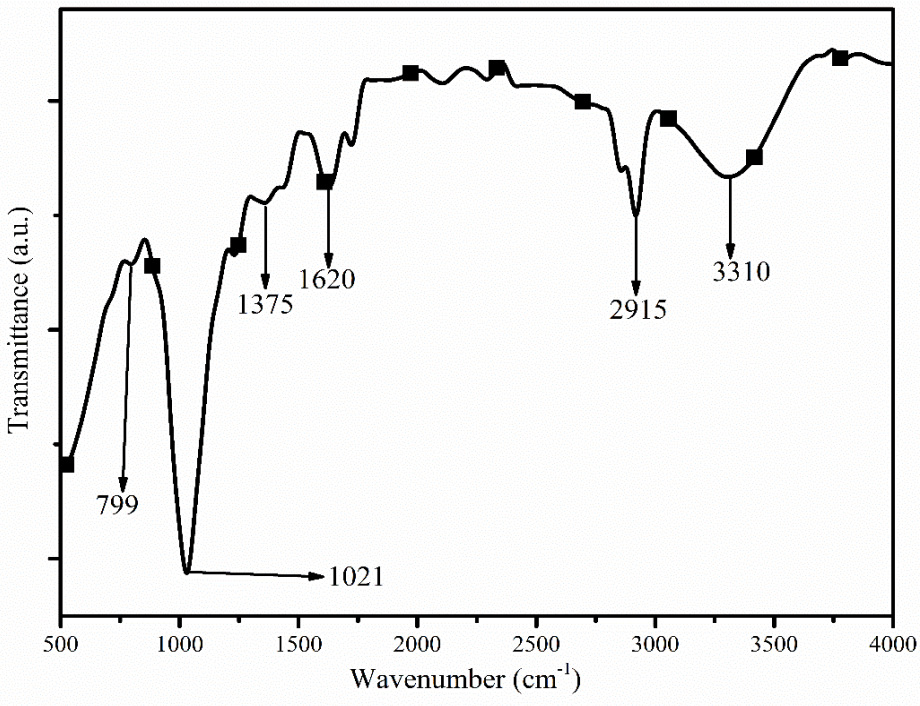


**Fig. 4.2:** Functional group analysis of LS biomass using FTIR analyzer

### 4.6.4 Thermal stability profile and influence of heating rates

The thermal stability analysis of LS biomass is used to understand the thermal conversion phenomenon and assess the kinetic parameters through different techniques. Fig. 4.3 (a) demonstrated the thermal stability profile of LS biomass at a 10 ℃/min heating rate in an inert atmosphere. The thermal decay profile of biomass demonstrated multistage decomposition and is divided into three main stages: moisture removal or drying zone, the second one is devolatilization or active pyrolytic zone, and the third one is char formation zone. During the first stage of decomposition of LS, the temperature varied from room temperature to 160 ℃, followed by the second stage (160 – 550 ℃) and the third stage (>550 ℃). A similar thermal decomposition profile was also stated by Mishra et al., [7] for the biomass (pine and sal sawdust, areca nut husk). Generally, the decomposition profile for most of the biomass occurs between 220 – 300℃ for hemicellulose, 300 – 340 ℃ for cellulose, and lignin between 300 – 900 ℃. Moreover, hemicellulose and cellulose decompose faster than lignin [60]. The decomposition of the first stage typically involves the discharge of moisture as well as certain

extremely volatile components of the LS biomass. However, a dramatic drop in the weight of LS was detected in the second stage (active pyrolysis region). This severe drop was due to the endothermic supply of heat, resulting in the fractionation of heavy molecular weight compounds into smaller molecular weight compounds [60]. The third stage involves the decomposition of lignin and other complex organic compounds attributed to their higher thermal stability. In fact, the thermal degradation of lignin was initiated at about 200°C during pyrolysis [8]. The breakdown of the lignin division ascribed to the C-O bond results in the product being formed with only one oxygen atom, while the methoxide division of the C-O bond increases two oxygen-containing products between 327 and 377 °C; however, side-chain C-C bond breakage occurs among the aromatic ring and the carbon particle [8]. Furthermore, biochar is formed as a result of the breakdown of comparably frail bonds (alkyl-aryl ether) under moderate reaction circumstances [8]. The differential thermogravimetric graph of LS biomass confirmed the removal of chemically bound moisture and lighted organic compounds in the 1$^{st}$ zone. The 2$^{nd}$ degradation zone (maximum decomposition) mainly revealed decay of cellulose and hemicellulose, whereas the 3$^{rd}$ zone mainly demonstrates biochar formation. Overall, LS decomposed around 8.6, 65, and 4.4% in first, second, and third stages, respectively.

The impact of dynamic heating rates has also been studied with the thermogravimetric analyzer under an inert ambiance. From Fig. 4.3 (b and c), the curve appears to change to the right side with an increment in the value of the heating rate from 10 to 40 °C/min due to the formation of thermal lag between biomass particles [95]. This happens due to a reduction in the interaction time among biomass (decreased residence time); thus, the transfer of heat is decreased and ultimately forms heat resistance between biomass particles (thermal lags) [101]. The DTG peak temperature changed from 350 to 362°C with an increment in the value of the heating rates. This impact arose from the thermal lags inside the specimen, generally causing restriction in

heat transfer during the process, enhancing volatilization of the biomass constituents [101]. By increment in the heating rate, several reactions occur within a shorter span of time, quickly reducing the initial mass of the biomass sample and leading to an increase in its temperature [102]. Upon increasing the heating rate (10 to 40℃/min), the curves shift towards the right, indicating that a higher temperature is required for the biomass to start the devolatilization process at a higher heating rate [102]. Still, the nature of the curve remains similar, and the overall reaction mechanism is independent of the heating rates [103]. From Fig. 4.3 (b and c), it is clear that quicker mass loss starts approximately at 175 and 205℃, pertaining to heating rates of 10 and 40℃/min, respectively.

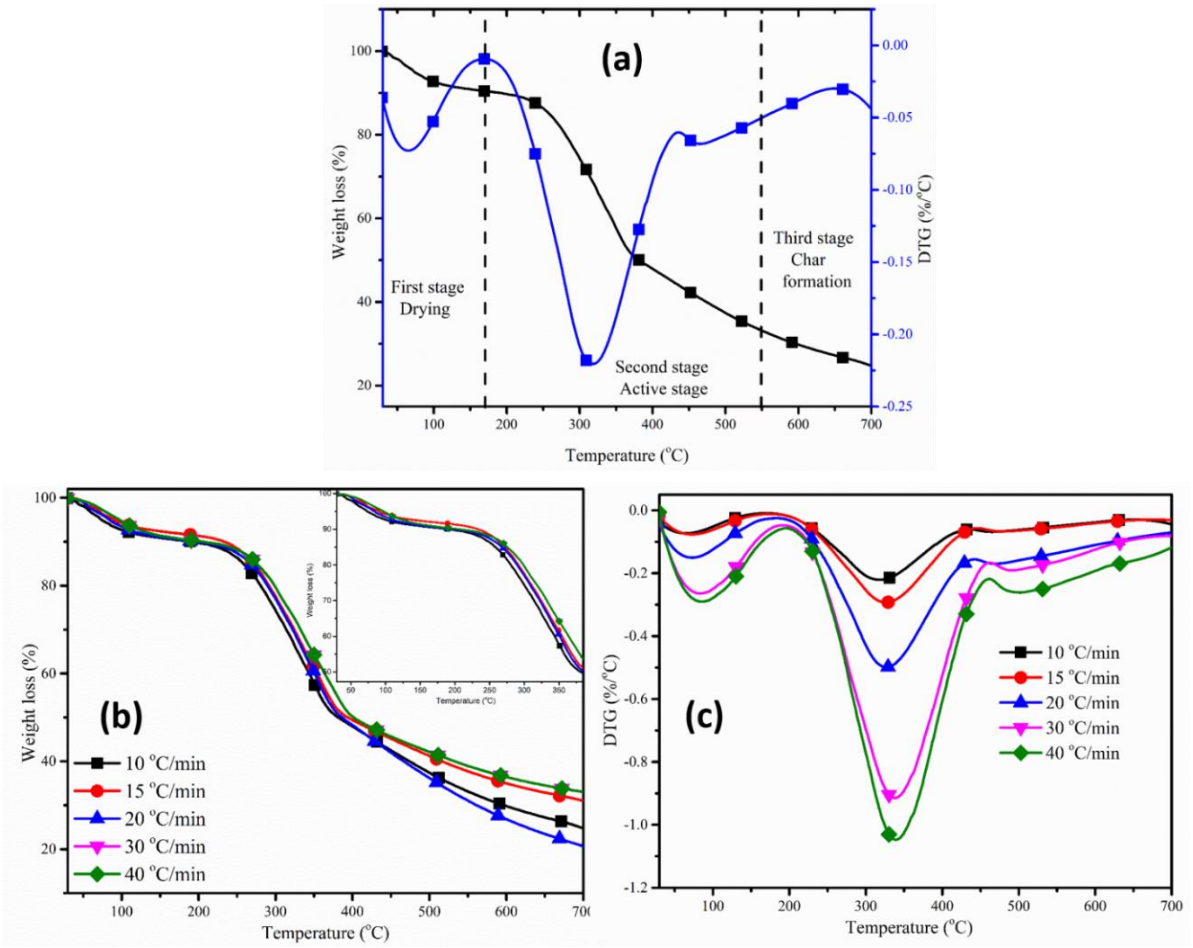


**Fig. 4.3 (a):** Thermal stability profile of LS biomass at 10 ºC/min heating rate, **(b)** Effect of dynamic heating rates on the TG profile, and **(c)** Effect of dynamic heating rates on the DTG profile

### 4.6.5 Kinetic analysis

The pyrolysis of biomass involves scores of complex reactions in series and parallel. The overall rate is governed by three important parameters: activation energy ($E_\alpha$), pre-exponential factor (A), and the appropriate thermodynamic factor. The kinetic parameters of LS biomass have been evaluated using five model-free methods, namely KAS, OFW, TM, ST, and VZK, and presented in Table 4.2. The pyrolysis experiment was performed within 30 – 700℃ temperature, and the curve fitting of the models was fitted within 0.1 to 0.7 conversion value, as seen in Fig 4.4. The low correlation coefficient value was incompatible with conversion values beyond 0.7 [105]. The average apparent activation energy gained from KAS, OFW, TM, ST, and VZK models were 117.68, 164, 154.63, 154.61, and 141.93 kJ/mol, respectively; however, more precisely, it varied from 69.28 – 117.68, 75.89 – 129.26, 69.53 – 118.12, 69.49 – 118.05, and 63.38 – 110.60 kJ/mol using KAS, OFW, TM, ST and VZK models respectively. The conversion range 0.1 – 0.7 was selected for the kinetic analysis due to the high correlation coefficient (greater than 0.90) for each model that showed the best fitting of the model with the experimental data (Table 4.2). The apparent activation energy gained through model-free methods has no physical meaning. Still, it can be rendered understandable through MCT (molecular collision theory) [106]. Based on the MCT, only a few specific molecules were affected during random pyrolysis, which enhanced their kinetic energy and permitted them to begin reactions that disrupted previous chemical bonds [8]. Such encounters can momentarily disrupt old chemical bonds and form new bonds, generating new molecules [8]. In addition, the reactivity of any fuel was determined as a result of its activation energy, forming an essential factor during pyrolysis, besides being pertinent to the design of pyrolyzer [95]. The analysis of kinetic parameters demonstrated that the activation energy has directly related to conversion and established that the LS went through a multifaceted pyrolysis reaction and is interconnected to miscellaneous reaction natures [61]. Fig. 4.5 portrayed the change in activation energy over progressive conversion. From Fig. 4.5, it can be seen that in the

conversion range 0.1 to 0.5, apparent activation energy increased; however, above conversion 0.5, the apparent activation energy decreased due to the fractionation of specific biomass products. The little difference in activation energy values of the respective model was due to diverse forms of assumption. Moreover, the difference in a chemical constituent of biomass, complex reactions, and charring also plays an important role in the variation of activation energies above 50% conversion value [105,107]. Fractionation of LS components such as hemicellulose, cellulose, and lignin also affects activation energy [8]. Furthermore, the change in activation energy may have been stimulated by the shape and size of the biomass constituents (hemicellulose, cellulose, and lignin). The weaker bonds of the biomass decomposed at a lower temperature and needed moderate energy, whereas the fractionation of the stronger bonds required higher energy and decomposed at a higher temperature [95].

The average activation energy gained from the kinetic study of LS using KAS, OFW, TM, ST, and VZK models exhibited good agreement when compared with Sugarcane leaves [108], Pine sawdust, Sal sawdust, and Areca nut husk [7], *Azadirachta indica* seeds, and *Phyllanthus emblica* kernels [95], and Banana trunk [110]. It is observed that the average activation energy of biomass varied significantly in content, decomposition temperature, and types of approximation [110]. It is also stated that the apparent activation energy of a fuel directly relates to fuel types, mathematical calculations, and operating conditions of the pyrolysis experiment [95]. Among all the adopted models in this study, VZK produced superior estimates of apparent kinetic parameters than KAS, OFW, TM, and ST. Our results are also supported by the ICTAC, an advanced isoconversional association that stated that VZK gives better results than other model-free methods [95]. Further, apart from VZK, KAS has a higher error, followed by OFW, ST, and TM due to implemented assumptions [111]. The present results also supported our hypothesis about the error of the models. Among all the tested models, VZK yielded a lower error.

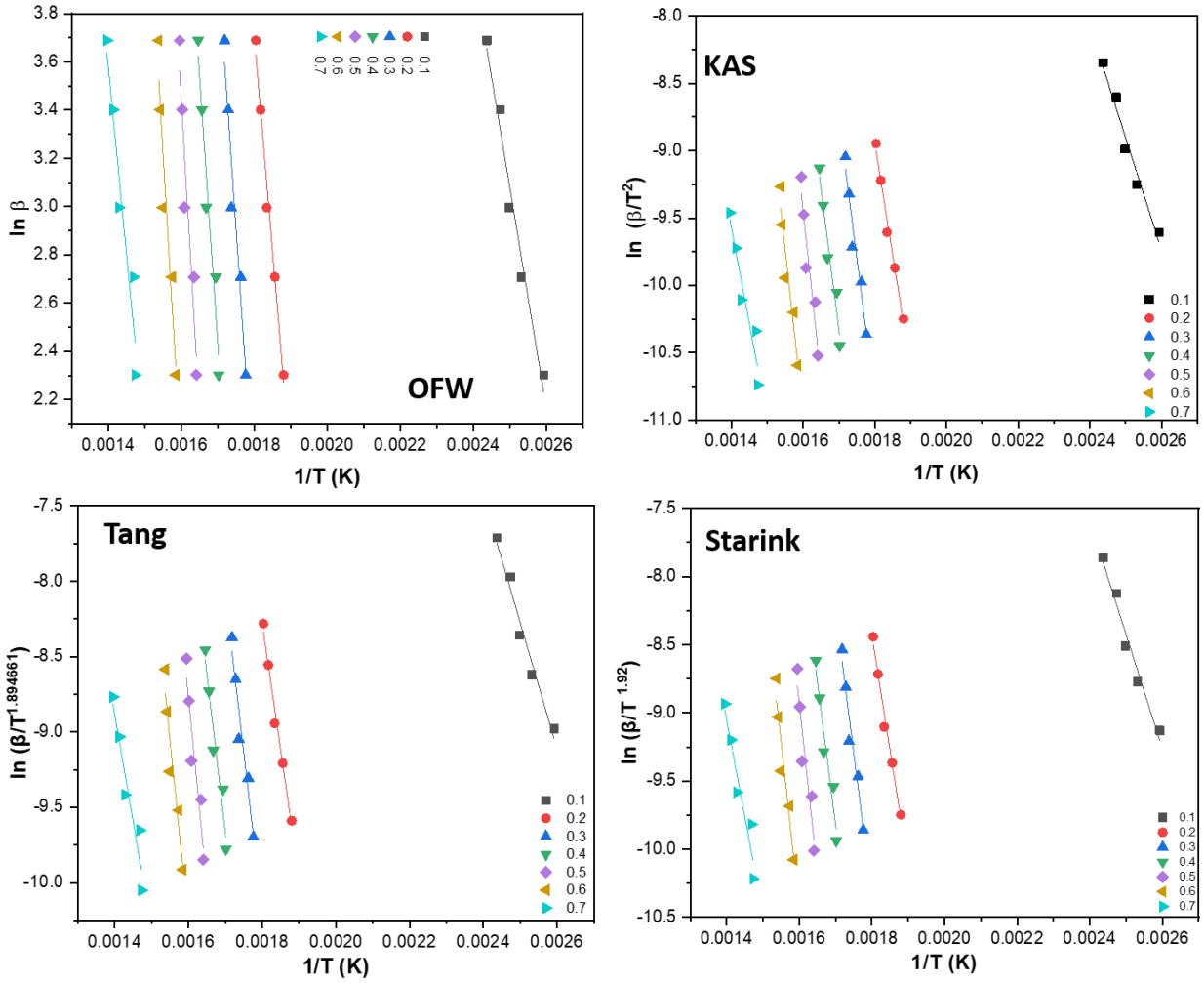


**Fig. 4.4:** Curve fitting of LS against model free methods

**Table 4.2:** Assessed and average activation energy values by different techniques from conversion

| Kinetic methods | | | | | | | | | | | | | |
|---|---|---|---|---|---|---|---|---|---|---|---|---|---|
| (α) | OFW | | KAS | | | Tang | | | Starink | | | Vyazovkin | |
| | E(kJ/mol) | $R^2$ | E(kJ/mol) | $R^2$ | Error (%) | E(kJ/mol) | $R^2$ | Error (%) | E(kJ/mol) | $R^2$ | Error (%) | E(kJ/mol) | Error (%) |
| 0.1 | 75.89 | 0.9742 | 69.28 | 0.9694 | 0.087 | 69.53 | 0.9697 | 0.083 | 69.49 | 0.9696 | 0.084 | 63.38 | 0.16 |
| 0.2 | 148.08 | 0.9881 | 139.06 | 0.9866 | 0.061 | 139.34 | 0.9867 | 0.059 | 139.31 | 0.9867 | 0.059 | 128.32 | 0.13 |
| 0.3 | 183.35 | 0.9541 | 173.84 | 0.9492 | 0.052 | 174.09 | 0.9495 | 0.050 | 174.08 | 0.9495 | 0.056 | 158.62 | 0.13 |
| 0.4 | 183.77 | 0.9536 | 173.84 | 0.9485 | 0.054 | 174.11 | 0.9488 | 0.052 | 174.10 | 0.9487 | 0.051 | 161.98 | 0.11 |
| 0.5 | 215.11 | 0.917 | 204.84 | 0.9093 | 0.048 | 205.08 | 0.9097 | 0.046 | 205.09 | 0.9096 | 0.047 | 187.44 | 0.12 |
| 0.6 | 212.56 | 0.9208 | 201.91 | 0.913 | 0.05 | 202.17 | 0.9134 | 0.048 | 202.17 | 0.9133 | 0.049 | 183.22 | 0.13 |
| 0.7 | 129.26 | 0.9344 | 117.68 | 0.922 | 0.09 | 118.12 | 0.9227 | 0.086 | 118.05 | 0.9226 | 0.087 | 110.6 | 0.14 |
| Mean | 164.00 | - | 154.35 | - | 0.063 | 154.63 | - | 0.061 | 154.61 | - | 0.057 | 141.93 | 0.13 |

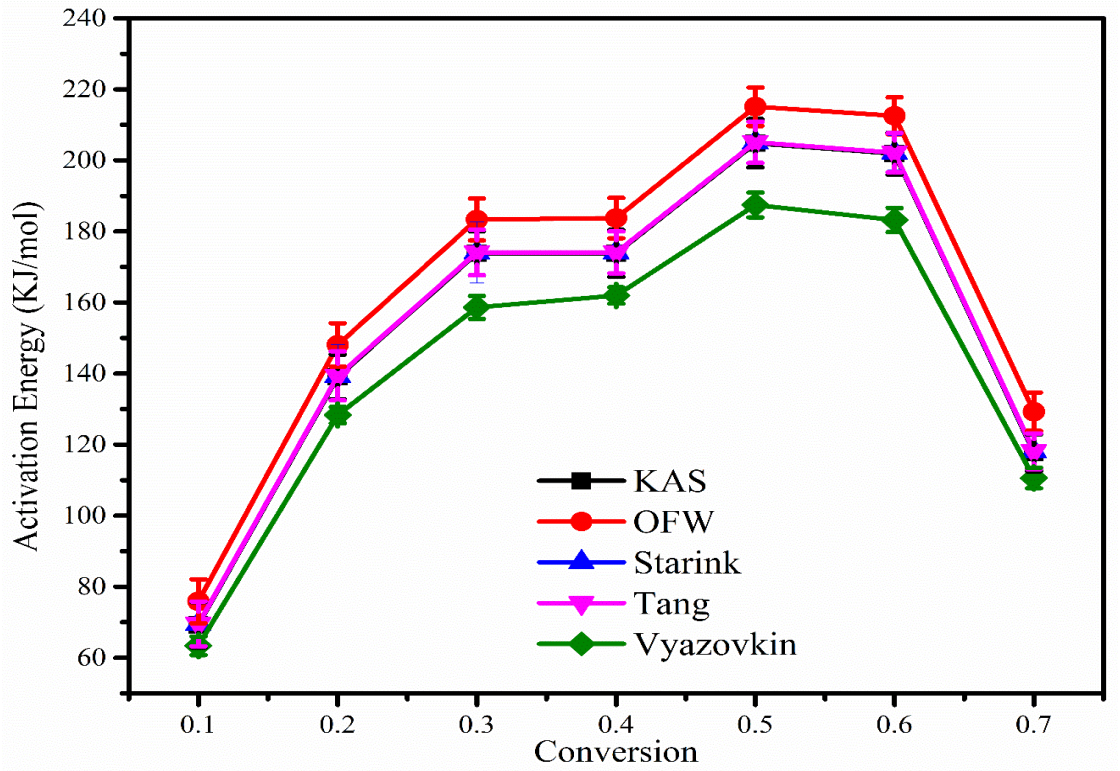


**Fig. 4.5:** Variation in activation energy value with respect to conversion

### 4.6.6 Evaluation of Reaction Mechanism

The values of activation energy obtained using VZK at the heating rate of 10°C/min were applied to evaluate the thermal degradation reaction mechanism of pyrolysis of LS by utilizing Criado's master plot method. The theoretical z(α) vs. conversion (α) curves were evaluated at different conversion values. The experimental curve was obtained using Eq. (3.21), and the theoretical curves were obtained by multiplying the f(α) and g(α) functions which are presented in Table 3.1. Fig. 4.6 represents the theoretical and experimental *z (α)* master plots for LS, which were utilized to predict the pyrolytic reaction mechanism by comparing the experimental and theoretical data curves. To determine the degradation of solid reaction processes, these theoretical curves are matched with experimental results. They have been divided into five main groups, each labeled as F, D, R, and A [86]. Where F stands for random nucleation on the individual particle, D stands for diffusion process connected with heat transfer capacity, R stands for phase boundary controlled reaction, and A stands for nucleation and growth

mechanism. It can be seen from Fig. 4.6 that the experimental curve overlaps the theoretical curve (D1, D2, and D3). According to testified literature, the breakdown mechanism in the diffusion technique was found in single, double, and three dimensions [86]. The findings indicate that diffusion mainly occurred throughout the pyrolysis at a lower conversion value. From conversion ranging from 0.1 to 0.2, the experimental z (α) curve is localized between D1 and D2 master curves, which are linked to one and two-dimensional diffusion mechanisms. From conversion ranging from 0.2 to 0.5, the experimental z (α) curve is close to the D1 master curve, which is linked to the one-dimensional diffusion mechanism. From 0.6 to 0.7 conversion, the experimental z (α) curve overlays the curve pertaining to D3, which corresponds to the diffusion process in three dimensions. It was also found that at over50 % conversion value, the F1 mechanism that corresponds to random nucleation with one nucleus in the distinct element will occur [86]. F1 mechanism, which occurs as decay, is given from random locations and performed as a growth center for the breakdown processes. As per the findings, at greater than 50% conversion, biomass constituents decayed into smaller molecules due to higher temperature. Smaller molecular mass chains are anticipated to function as centers of random nucleation and growth for decay processes.

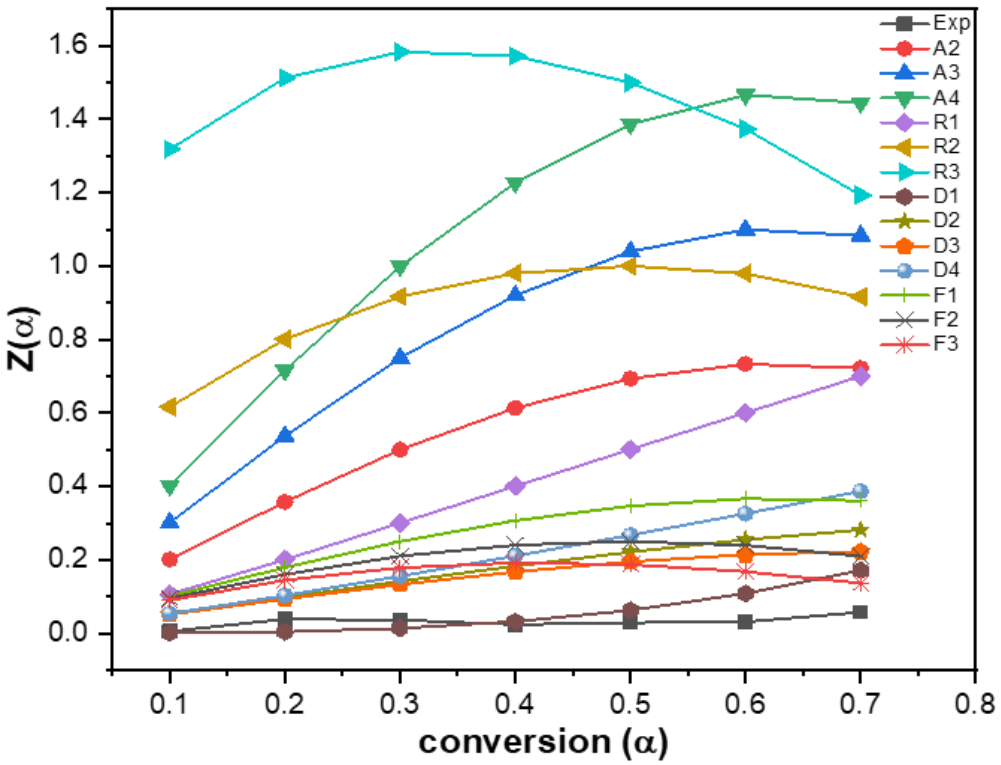


**Fig. 4.6:** Theoretical and experimental plots for prediction of solid-state reaction mechanism using Criado method (Z-master plot)

### 4.6.7 Thermodynamic Parameters

Thermodynamic parameters of LS biomass were estimated based on activation energy gained via VZK, KAS, and OFW at the heating rate of 10℃/min and are listed in Table 4.3. Thermodynamic parameters were estimated at a lower heating rate due to smooth interactions between the constituents during the pyrolysis [94]. The range of pre-exponential values obtained from the VZK, KAS, and OFW methods varied from $10^4 – 10^{10}$, $10^4 – 10^{15}$, and $10^4 – 10^{14}$ $s^{-1}$. The excessively large value of pre-exponential factor $>10^9$ $s^{-1}$ indicates the formation of the chemical complex in LS biomass prior to the formation of final products, a result of the complicated parallel chemical reactions occurring during the process of pyrolysis [106]. From the initial pyrolysis to the final products, the pre-exponential factor varied significantly due to the extra energy needed to initiate the breakdown of hemicellulose and cellulose at the start of

the pyrolytic process; subsequently, when the energy barrier is overcome, the deterioration of LS requires lower energy [106].

Enthalpy is a well-known thermodynamic parameter describing the heat content of the entire system, and the change in the value of enthalpy (ΔH) is the difference in energy between activated complex and biomass. In the case of pyrolytic processes, enthalpy signifies the overall energy that the biomass consumes for transformation into different products such as bio-oil, bio-gas, and bio-char [110]. The findings showed that a slight change in activation energy and enthalpy (3 – 7 kJ/mol) was due to energy variance among the reagents and activated complex, which lifts the development of the activated complex [112]. The difference in activation energy and enthalpy value is varied from 3-7 kJ/mol, which means that product formation can be achieved by supplying a small amount of supplementary energy [113].

Gibb's free energy (ΔG) obtained from VZK, OFW and KAS are 165.10 – 165.87, 162.85 – 165.06, and 168.30 – 156.55 kJ/mol, respectively, indicating a comparatively strong energy production throughout the process. Thermodynamic parameters are a crucial constraint in the thermochemical renovation of biomass for the assortment of the appropriate biomass as well as for the suitable design of a pyrolysis reactor in the large-scale pyrolysis process [95].

Entropy is a state function representing the randomness of the system. The change in entropy (-ve sign) implies that the degree of disorderness of products generated by bond dissociations was less than that of the initial reactants. The average value of ΔS gained from VZK, OFW, and KAS are -7.75, -23.78, and -44.39 J/mol.K, respectively. It indicates that more biomass components are volatilized because LS is thermally deteriorating in an inert atmosphere. The significant change in entropy moved the sample into physicochemical aging, bringing it closer to thermodynamic parameters equilibrium, reducing reactivity, and taking a longer time to create the activated complex.

**Table 4.3:** Thermodynamic parameters for LS biomass based on OFW, KAS and Vyazovkin

| Model | Conversion (α) | Frequency factor, A (1/s) | Enthalpy (kJ/mol) | Gibbs free energy (kJ/mol) | Entropy (J/mol.K) |
|---|---|---|---|---|---|
| OFW | 0.1 | 2.55057E+5 | 72.68 | 167.82 | -152.68 |
| | 0.2 | 5.6026E+11 | 143.65 | 164.36 | -33.22 |
| | 0.3 | 6.2767E+14 | 178.67 | 163.25 | 24.73 |
| | 0.4 | 6.8224E+14 | 178.88 | 163.24 | 25.09 |
| | 0.5 | 3.38414E+17 | 210.04 | 162.43 | 76.40 |
| | 0.6 | 2.04415E+17 | 207.31 | 162.49 | 71.92 |
| | 0.7 | 1.29342E+10 | 123.61 | 165.06 | -66.52 |
| | Average | 7.77342E+16 | 159.26 | 164.09 | -7.75 |
| KAS | 0.1 | 6.50080E+4 | 66.07 | 168.30 | -164.04 |
| | 0.2 | 9.22528E+10 | 134.64 | 164.69 | -48.22 |
| | 0.3 | 9.49326E+13 | 169.16 | 163.53 | 9.02 |
| | 0.4 | 9.49326E+13 | 168.95 | 163.53 | 8.69 |
| | 0.5 | 4.43919E+16 | 199.77 | 162.68 | 59.51 |
| | 0.6 | 2.48562E+16 | 196.66 | 162.75 | 54.40 |
| | 0.7 | 1.25970E+9 | 112.03 | 165.55 | -85.88 |
| | Average | 9.91973E+15 | 149.61 | 164.43 | -23.78 |
| Vyazovkin | 0.1 | 1.904294E+4 | 60.17 | 168.76 | -174.25 |
| | 0.2 | 1070962E+4 | 123.89 | 165.10 | -66.13 |
| | 0.3 | 4.58969E+12 | 153.94 | 164.00 | -16.15 |
| | 0.4 | 8.96487E+12 | 157.09 | 163.90 | -10.92 |
| | 0.5 | 1.41309E+15 | 182.37 | 163.14 | 30.85 |
| | 0.6 | 6.11690E+14 | 177.97 | 163.26 | 23.60 |
| | 0.7 | 3.018758E+8 | 104.95 | 165.87 | -97.76 |
| | Average | 2.91192E+14 | 137.20 | 164.86 | -44.39 |

### 4.6.8 Compensation effect

The connection between activation energy and logarithmic pre-exponential factors for LS biomass pyrolysis was investigated at various fractional conversion levels based on OFW, KAS, and VZK methods. As shown in Fig. 4.7, a compensation effect can be seen from the beginning to the final value of conversion with $R^2$ close to unity. At the molecular level, an increase in temperature increases the vibration among the particles, causing molecules to stretch and bend more. The correlation between activation energy and logarithmic pre-exponential factor is linear because the reaction rate is assumed to obey an Arrhenius-type law [114,115]. The plot depicts (Fig. 4.7) a linear pattern with high fitting accuracy close to unity, indicating that the calculated kinetic parameters are valid.

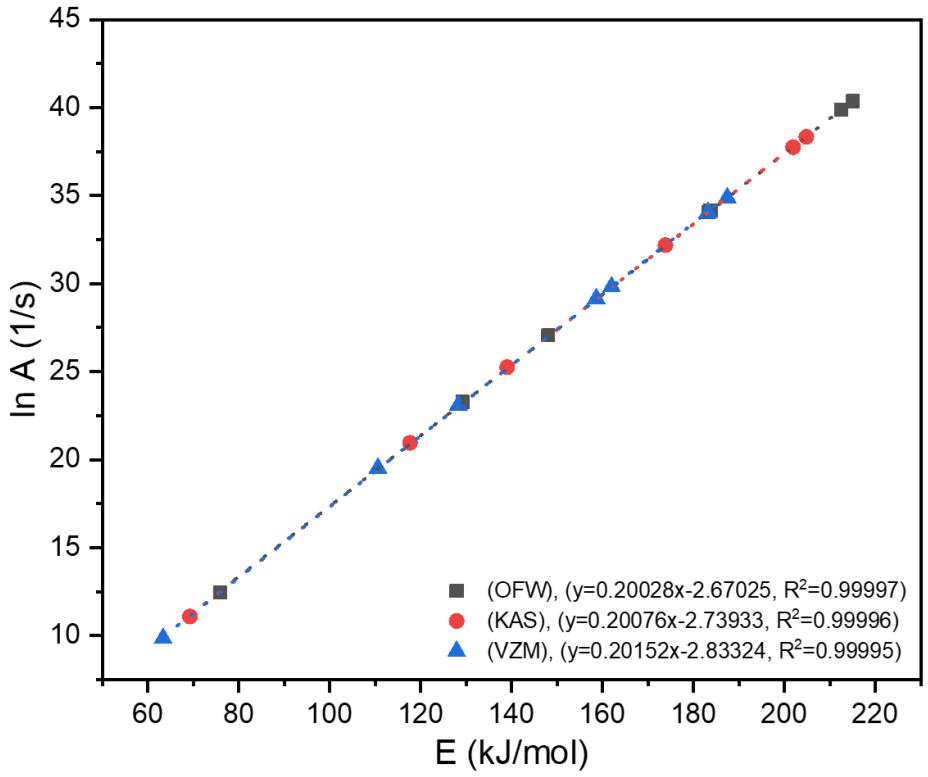


**Fig. 4.7:** Correlation between activation energy and pre-exponential factor of LS biomass

### 4.6.9 Pyrolysis parameter optimization using RSM

The simultaneous effect of process response and independent variables was investigated using response surface methodology (RSM) based on a central composite design (CCD) approach.

The bio-oil yield was chosen as the process response in this study, with temperature, heating rate, and $N_2$ flow rate as an independent variable. According to the DE software's recommendations, 20 experimental runs were carried out, with 6, 8, and 6 axial, factorial, and center points, respectively. Table 4.4 shows the complete experimental design matrix and response. The following coded factors reflected the link between the dependent factor and the independent factors:

$$Bio-oil\ yield\ (wt\ \%) = +43.48 + 2.35A + 1.57B - 4.07C - 3.56A^2 - 2.19B^2 - 3.43C^2 - 0.6453AB + 0.5148AC - 0.4107BC$$

The coded parameters A, B, and C signify temperature, heating rate, and $N_2$ flow rate, respectively. The bio-oil yield ranged from 32.5 to 45.6%, although the optimum temperature, heating rate, and $N_2$ flow rate for the maximum bio-oil production were 550°C, 65°C/min, and 60 ml/min, respectively. Table 4.5 displays the results of the ANOVA. F and p-value are used to measure the influence of each independent variable on the outcome at a 95% confidence interval. For bio-oil yield, the F value is 135.09, and the p-value is <0.0001, showing that the constructed model is suitable. Considering the linear and quadratic components leads to the conclusion that factors A, B, AB, $A^2$, $B^2$, and $C^2$ were significant since the value of p was less than 0.0500. (Table 4.5). The higher p-values of C, AC, and BC govern that the terms are insignificant. The temperature has a bigger F-value (55.85) than the heating rate (8.03) and $N_2$ flow rate (4.86), implying that temperature has a greater impact on bio-oil output than the $N_2$ flow rate and heating rate. Furthermore, it was discovered that interaction terms such as AB, AC, and BC had little effect on bio-oil output due to lower F-values. The F-values of $A^2$, $B^2$, and $C^2$ were 122.43, 9.43, and 1.03, respectively, demonstrating that $A^2$ (temperature) has a more significant impact on pyrolytic liquid yield.

The objective of the three-dimensional plot is to categorize the surface shape for a range of factors employed, as well as to demonstrate the efficiency of the various variables on bio-oil

production [116,117]. The contour plot of the close-fitting model is the most meaningful and easiest approach to characterize the response surface. Furthermore, reducing the number of process variables to two or three simplifies contour plot development and interpretation [80,118]. The current research looks at the impact of three process factors on the yield of pyrolysis products. It is virtually hard to depict all the impacts in the same three dimensions and counterplots. As a consequence, one parameter remained constant while the others were altered. Fig. 4.8 (a, b, and c) depicts the consequence of process factors such as temperature, heating rate, and flow rate of $N_2$ on bio-oil output. As shown in Fig. 4.8 (a), bio-oil yield increased as the temperature enhanced from 400 to 550°C, but as the temperature increased more, it began to fall. It can be shown in Fig. 4.8 (a) that when the heating rate was enhanced from 20 to 65°C/min, the bio-oil production increased, but as the heating rate was increased further, the yield began to fall. The related contour plot likewise yielded similar findings. The influence of temperature and $N_2$ flow rate on bio-oil output was depicted in Fig. 4.8 (b). It has been addressed how temperature affects bio-oil output. The figure shows that increasing the flow rate of $N_2$ from 50 to 60 ml/min increased liquid product output, but any further increase lowered it. The impact of heating rate and $N_2$ flow rate on bio-oil output was depicted in Fig. 4.8 (c). The bio-oil output rose as the heating rate enhanced from 20 to 65°C/min, as shown in Fig. 4.8 (c); however, when the heating rate went further, the yield began to diminish. Increasing the $N_2$ flow rate from 50 to 60 ml/min, on the other hand, boosted bio-oil output, but any further increase decreased it. Furthermore, Fig. 4.8 (a, b, and c) revealed that the influence of temperature was greater than the influence of heating rate and flow rate of $N_2$, whereas the influence of $N_2$ flow rate was minimal in contrast to heating rate and temperature. The link between the actual and predicted values is depicted in Fig. 4.9. It shows that the actual value is very near to the expected value, with $R^2$ value of 0.9918, showing that the chosen model was effective and competent for comprehending the impacts of the pyrolysis process.

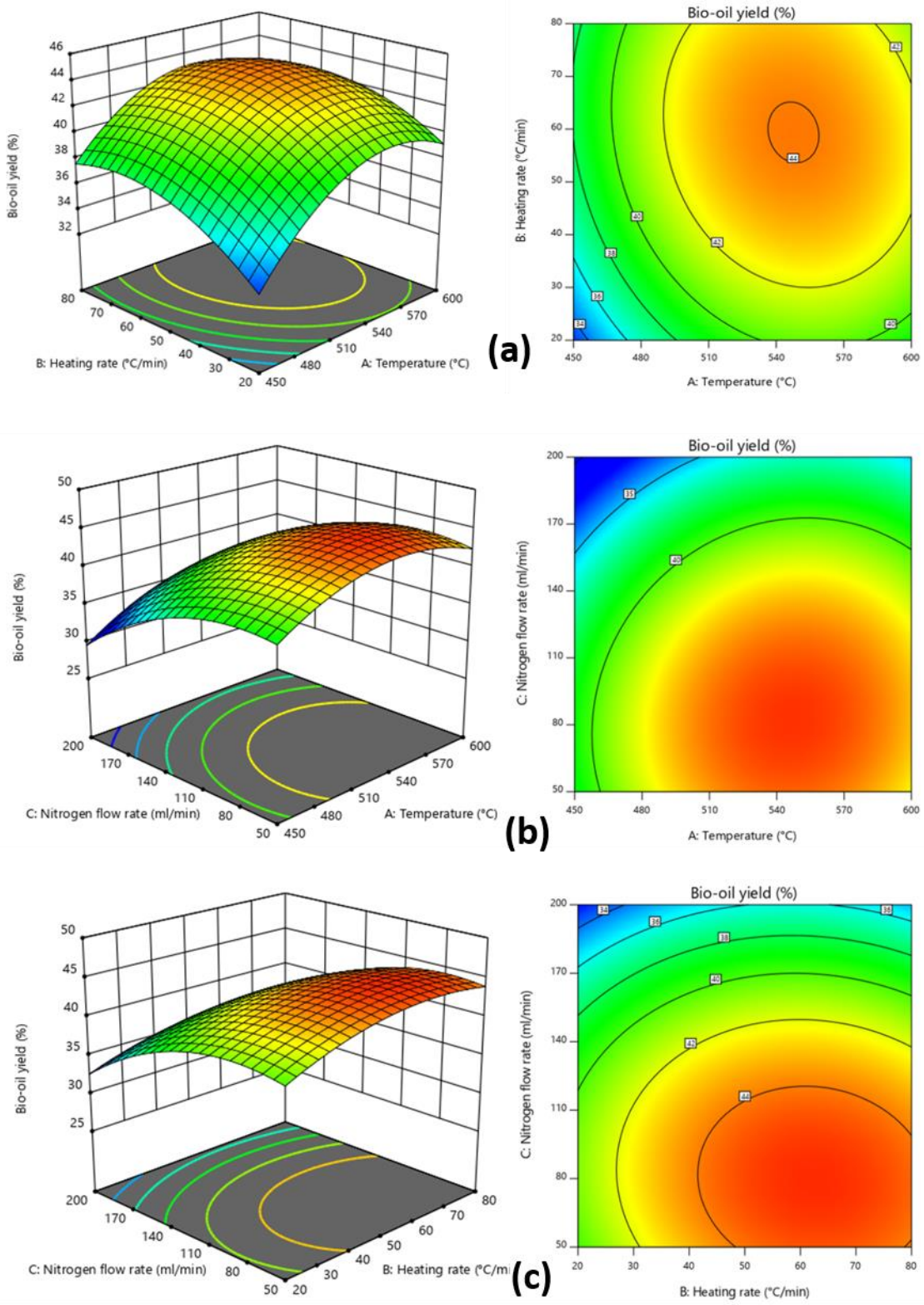


**Fig. 4.8:** 3-Dimensional response surface and contours plots of bio-oil production vs **(a)** heating rate and temperature **(b)** flow rate of $N_2$ and temperature **(c)** heating rate and inert gas ($N_2$) flow rate

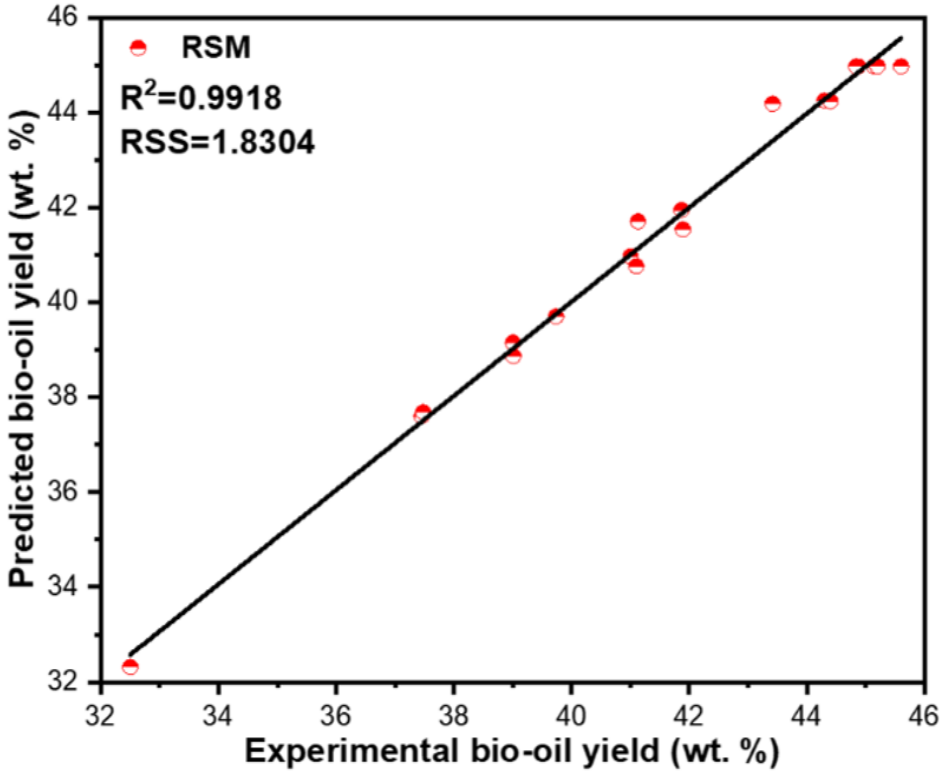


**Fig. 4.9:** Experimental and predicted bio-oil yields

**Table 4.4:** Actual and expected response values based on experimental design matrix

| Run | Factor 1 A:Temperature (°C) | Factor 2 B:Heating rate (°C /min) | Factor 3 C:sweeping gas flow rate (ml/min) | Response | |
|---|---|---|---|---|---|
| | | | | Predicted bio-oil yield (%) | Actual bio-oil yield (%) |
| 1 | 450 | 40 | 50 | 37.60 | 37.45 |
| 2 | 550 | 65 | 120 | 44.25 | 44.3 |
| 3 | 400 | 65 | 60 | 32.32 | 32.5 |
| 4 | 620 | 40 | 100 | 40.97 | 41 |
| 5 | 450 | 40 | 100 | 37.69 | 37.48 |
| 6 | 550 | 65 | 60 | 44.98 | 45.6 |
| 7 | 630 | 65 | 50 | 39.71 | 39.74 |
| 8 | 600 | 80 | 50 | 41.54 | 41.89 |
| 9 | 550 | 65 | 60 | 44.98 | 45.14 |
| 10 | 550 | 65 | 60 | 44.98 | 45.2 |
| 11 | 600 | 80 | 100 | 41.94 | 41.87 |
| 12 | 550 | 80 | 60 | 44.19 | 43.42 |

| | | | | | |
|---|---|---|---|---|---|
| 13 | 450 | 80 | 100 | 38.87 | 39.01 |
| 14 | 550 | 20 | 60 | 40.77 | 41.1 |
| 15 | 550 | 65 | 60 | 44.98 | 44.87 |
| 16 | 550 | 65 | 60 | 44.98 | 44.85 |
| 17 | 550 | 65 | 60 | 44.98 | 44.84 |
| 18 | 450 | 80 | 50 | 39.15 | 39 |
| 19 | 550 | 65 | 40 | 44.24 | 44.4 |
| 20 | 600 | 40 | 50 | 41.71 | 41.13 |

**Table 4.5:** Analysis of variance (ANOVA) for the quadratic response model: Bio-oil

| Source | Sum of squares | df | Mean square | F-value | p-value | Remark |
|---|---|---|---|---|---|---|
| **Model** | 224.37 | 9 | 24.93 | 135.09 | <0.0001 | Significant |
| A-Temperature | 10.31 | 1 | 10.31 | 55.85 | <0.0001 | |
| B-Heating rate | 1.48 | 1 | 1.48 | 8.03 | 0.0177 | |
| C-Sweeping gas flow | 0.8974 | 1 | 0.8974 | 4.86 | 0.0520 | |
| AB | 1.61 | 1 | 1.61 | 8.72 | 0.0145 | |
| AC | 0.3134 | 1 | 0.3134 | 1.70 | 0.2217 | |
| BC | 0.0712 | 1 | 0.0712 | 0.3860 | 0.5483 | |
| $A^2$ | 122.43 | 1 | 122.43 | 663.39 | <0.0001 | |
| $B^2$ | 9.43 | 1 | 9.43 | 51.11 | <0.0001 | |
| $C^2$ | 1.03 | 1 | 1.03 | 5.57 | 0.0400 | |
| **Residual** | 1.85 | 10 | 0.1846 | | | |
| Lack of Fit | 1.40 | 5 | 0.2805 | 3.17 | 0.1158 | Not significant |
| Pure Error | 0.4429 | 5 | 0.0886 | | | |
| $R^2$ | 0.9918 | | | | | |
| **Cor. Total** | 226.22 | 19 | | | | |

### 4.6.10 Physicochemical characterization of the bio-oil

The physicochemical characteristics of LS bio-oil at optimized pyrolysis conditions are presented in Table 4.6 and compared with diesel and gasoline fuel. The obtained bio-oil has brown color and smoky smell. The nature of bio-oil was highly acidic (Table 4.6). The high acidity of bio-oil was due to the presence of significant number of organic acids. This implies that bio-oil will need to be significantly improved before it can be utilized as a liquid fuel. Increasing bio-oil quality prevents corrosion in storage and transportation pipelines [65]. The density of the bio-oil was determined to be 911 kg/m$^3$, which is somewhat higher than the density of diesel fuel. The bio-oil has a viscosity of 3.55 cSt, equivalent to diesel fuel but greater than gasoline. The viscosity of a substance indicates how easy or difficult it is to flow. High viscosity indicates complexity in flow, whereas low viscosity indicates flexibility in flow [119,120]. The fuel viscosity is vital in its injection and design [121]. The ash content of the bio-oil was determined to be 0.43 wt. %, while the calorific value of the bio-oil was determined to be 15.99 MJ/kg, which is significantly lower than diesel and gasoline fuel. The lower HHV value was attributed to the increased bio-oil acidity. Ramsbottom carbon residue, which was 2.15%, characterized the carbon-making propensity of pyrolytic liquid at increased temperature.

**Table 4.6:** Physicochemical characterization of LS bio-oil and compared with gasoline and diesel fuel

| Analysis | LS bio-oil | Gasoline | Diesel |
|---|---|---|---|
| Color | Brown | – | – |
| Smell | Smoky | – | – |
| Acidity | 2.55±0.21 | – | – |
| Density(kg/m$^3$) | 911.91±2.03 | 838 | 828 |
| Viscosity (cSt) (30 °C) (50 rpm) | 3.55±0.37 | 0.12 | 2–4 |
| Ash Content (wt. %) | 0.43±0.02 | – | – |
| HHV (MJ/kg) | 15.99±0.22 | 47.3 | 44.5 |

| | | | |
|---|---|---|---|
| Ramsbottom carbon residue (wt. %) | 2.15±0.07 | – | – |

### 4.6.11 FTIR analysis of bio-oil

FTIR spectroscopy was used to identify functional groups in the LS bio-oil (Fig. 4.10). The presence of alcohol, water, protein, and phenol was identified due to the linkage of –OH group at 3350 $cm^{-1}$ [117]. The presence of –CH stretching of alkane and –CN group of aliphatic cyanide and nitriles caused the bands at 2952 and 2160 $cm^{-1}$, respectively [99]. The existence of hemicellulose carbonyl group is revealed by the peak at 1638 $cm^{-1}$, while the existence of ester was established at peak (1389 $cm^{-1}$) due to C–O stretching and distortion [122]. The band peak (1270 $cm^{-1}$) was due to –CH stretching vibrations indicating alkane, whereas the band peak at 1029 $cm^{-1}$ indicated the presence of esters and ethers due to C=O stretching vibrations [123]. The presence of polycyclic aromatic components in the liquid product was demonstrated by the peak at 673 $cm^{-1}$.

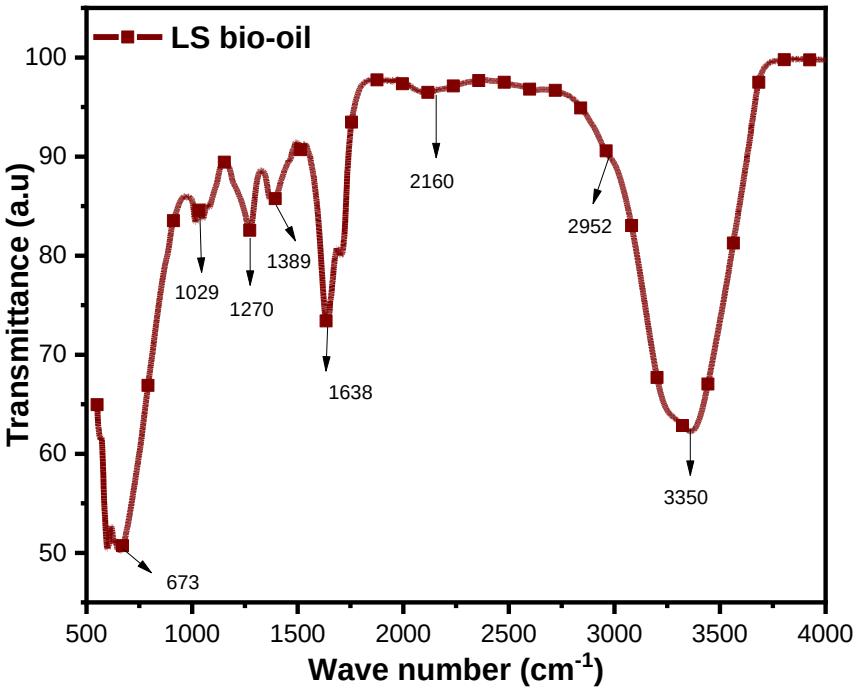


**Fig. 4.10:** FTIR analysis of the LS bio-oil

### 4.6.12 GCMS analysis of bio-oil

GCMS analysis (Fig. 4.11) of the LS bio-oil was carried out at optimized pyrolysis conditions and matched with the NIST library database to identify unknown organic components in the pyrolytic liquid. A detailed list of the compound identified are presented in Appendix D. It is generally known that bio-oil is a complex mixture of mostly acids, phenols, hydrocarbons, esters, ethers, ketones, alcohols, nitrogen-containing, etc., making bio-oil ideal for different applications [124]. However, it is important to note that the content of these chemicals varies greatly depending on the kind of biomass, feed mix, pyrolysis type, operating circumstances, and so on. The results revealed that the LS bio-oil contains hydrocarbons (22.67%), acids (10.53%), ketone (31.4%), esters (3.73%), alcohols (12.83%), $N_2$ containing (3.35%), and some other compounds (15.49%). These compounds have different industrial applications. For e.g., docosane can be employed in calibration, organic synthesis, and temperature sensor devices [117]. 1, 2-Benzene dicarboxylic acid, di isooctyl ester can be used as a plasticizer for polyvinyl chloride jackets for building wire. 3-Octen-2-ol, E- can be used in the fragrance industry. In addition, $N_2$ compounds in the bio-oil may result in NOx during engine operation or combustion. The findings suggest that pyrolytic liquid can be employed in household cooking or as a source of essential chemicals. However, further treatment (catalytic cracking) is necessary to enhance fuel quality and minimize corrosivity before it can be utilized as a diesel substitute.

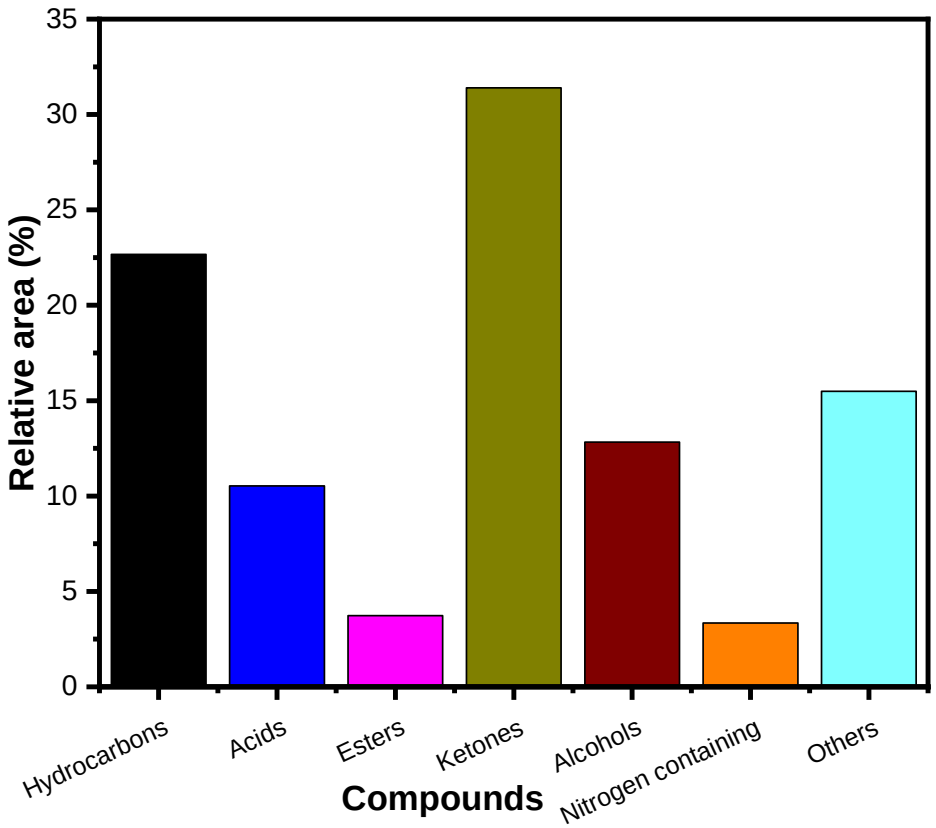


**Fig. 4.11:** GCMS analysis of the LS bio-oil

### 4.6.13 1H-NMR analysis of bio-oil

The existence of distinct kinds of protons in bio-oil centered on the chemical shift (CS) with the specified areas was determined through 1H-NMR (Fig. 4.12). 1H-NMR spectra are classified into three zones based on chemical shifts caused by distinct proton types: aliphatic, aromatic, and olefinic. Aliphatic resonances have a CS of 0.5 – 3.0 ppm, olefinic resonance has a CS of 4.5 – 6.3 ppm, and aromatic resonance has a CS of 6.0 – 9.0 ppm [125]. The initial area between 0.5 – 1.8 ppm resonates with roughly 50.13% of protons because of aliphatic hydrocarbon chains [126]. The 1.8 – 3.0 ppm spectra comprise 5.65% of the aliphatic protons connected to C=C, either olefinic or aromatic or two bonds abroad from heteroatom [127]. The 3 – 4.5 ppm spectra comprise 7.88% protons linked to amines, aliphatic alcohol, or a methylene group connecting two aromatic rings [128]. The presence of protons (23.32%) bound to carbon

atoms in the phenolic (OH) group or methoxyl, carbohydrate-type compounds, or olefin may explain the range of 4.5 – 7 ppm [127,128].

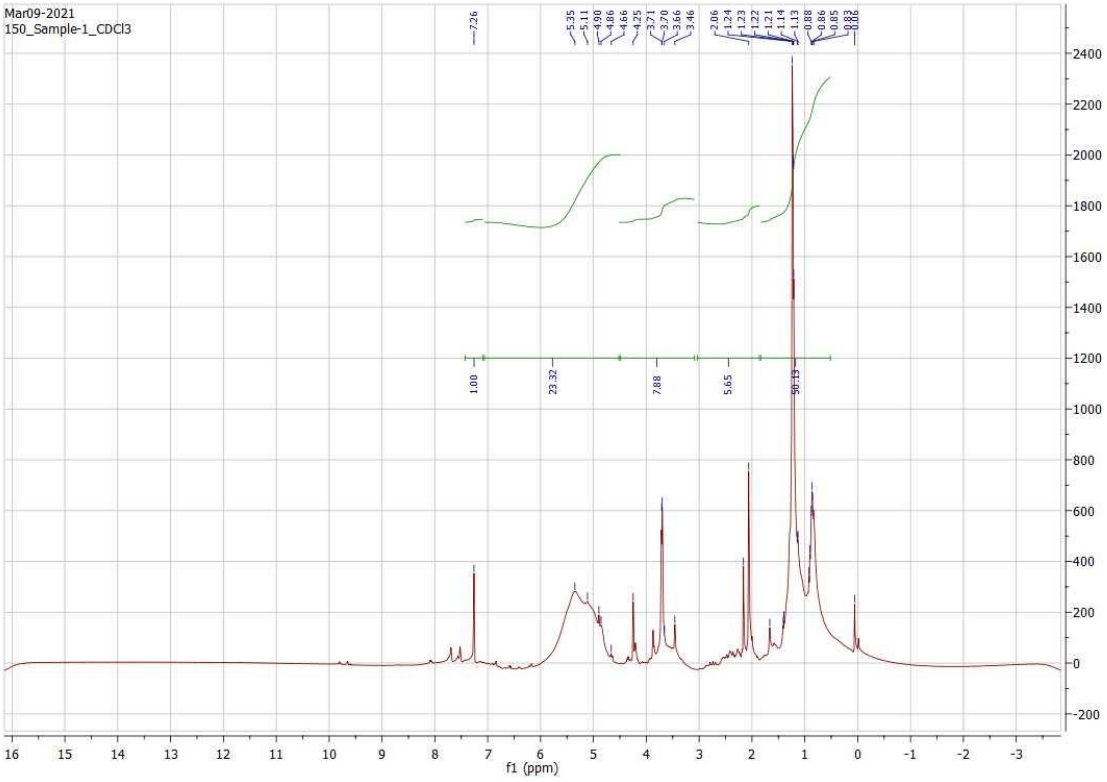


**Fig. 4.12:** 1H-NMR analysis of LS bio-oil

### 4.6.14 Physicochemical characterization of biochar

Biochar is the solid residue left after pyrolysis that has a wide range of applications and has been classified depending on characterization results. LS biochar obtained at optimized pyrolysis condition was further compared with *Samanea saman* seed biochar, coal, and torrefied *Acacia nilotica* and presented in Table 4.7. The findings of the proximate analysis revealed decreased moisture (2.67%), volatile matter (35.68%), and ash content (9.08%), but greater fixed carbon content (52.57%), which has a variety of industrial uses. The igniting efficiency of biochar with lower moisture and ash concentration is greater. Biochar may be stored for longer when moisture levels are lower [129]. Biochar with a greater ash content has a lower calorific value and acts as a heat sink, whereas lower ash concentration results in less slagging and fouling during boiler operations. The ultimate analysis revealed a significant

increase in carbon (43.45%) than raw biomass (38.94%). The significant increase in carbon content for the LS biochar was due to the release of the –OH functional group might be attributed to dehydration reaction. The decrease in nitrogen, oxygen, and hydrogen is due to the breaking of nitrile group and release of gases such as NOx during the course of pyrolysis [88,130]. Lower nitrogen concentration offers both benefits and drawbacks. Lower nitrogen level in biochar creates less NOx issue during burning; however, it also has limited utility when the major goal of biochar is to employ it in soil enhancement [131]. The HHV of the LS biochar was found to be 17.77 MJ/kg, slightly greater than the raw biomass. This is linked to the dispersion of volatiles and also due to an increase in carbon and a decrease in oxygen content [88]. The bulk density of biochar was found to be 503.3 kg/$m^3$, confirming that storage and transportation will be simpler. Surface area is a crucial consideration when using biochar as an adsorbent. The BET surface area of biochar was determined to be 16.19 $m^2$/g, which is less than that of activated carbons (800 $m^2$/g), indicating that it has limited value as a bio-adsorbent. The biochar's zeta potential was determined to be -32.43 mV, and its acidity was 9.42, promoting its use as a fertilizer/soil enhancer. Further, Van-Krevelen diagram (Fig. 4.13) was employed to determine the energy content in the biochar on the basis of molar ratios (O/C and H/C) and has been compared with *Samanea saman* seed biochar [63], torrefied *Acacia nilotica* [132], coal char [63], pea nutshell biochar [68], *Manilkara zapota* seed biochar [62], coffee husk biochar [98], palm shell hydrochar [129], and corncob biochar [133]. The results revealed that LS biochar has higher atomic ratios (lower energy content) in comparison to other reported biochars in this study. The surface morphology of the LS biochar was further investigated by FE-SEM and EDX, as shown in Fig. 4.14 (a and b). The findings indicated that C and O are the primary constituents in biochar, with other elements being N, Ca, and Si. In the pyrolysis process, these mineral matter act as a catalyst. The shape of the biochar was dramatically changed as a result of mineral component deposition (EDX analysis). The surface form of

biochar is altered as a result of numerous processes (de-hydration, de-carbonylation, and de-carboxylation) that occur during pyrolysis [134]. Furthermore, some pores and cracks were discovered as a result of raw material deterioration and volatilization during heat treatment [129].

**Table 4.7:** Physicochemical characterization of LS biochar along with other reported biochar

| Analysis | LS biochar | *Samanea saman* seed biochar [63] | Torrefied *Acacia nilotica* [132] | Coal [63] |
|---|---|---|---|---|
| Proximate analysis (wt. %) | | | | |
| Moisture | 2.67±0.18 | 5.14 | 0.85 | – |
| Ash Content | 9.08±0.79 | 13.18 | 2.39 | – |
| Volatile matter | 35.68±0.76 | 34.14 | 40.15 | – |
| Fixed carbon* | 52.57 | 47.54 | 56.61 | – |
| Ultimate analysis (%) | | | | |
| C | 43.45 | 62.66 | 63.75 | 55.38 |
| H | 4.85 | 2.06 | 2.62 | 5.86 |
| N | 0.95 | 3.45 | 2.14 | 2.48 |
| S | – | – | – | 2.21 |
| O* | 50.85 | 31.83 | 31.49 | 34.07 |
| O/C | 0.87 | 0.38 | 0.49 | |
| H/C | 1.34 | 0.39 | 0.04 | |
| Heating value (MJ/kg) | 17.77±0.03 | 23.14 | 25.94 | 22.54 |
| Bulk density (kg/m$^3$) | 503.3±1.33 | 478 | – | – |
| Acidity | 9.42±0.10 | 7.60 | – | – |
| BET surface area (m$^2$/g) | 16.19 | 8.20 | – | – |
| Zeta potential (mV) | -32.43±1.4 | – | – | – |

*On the difference basis

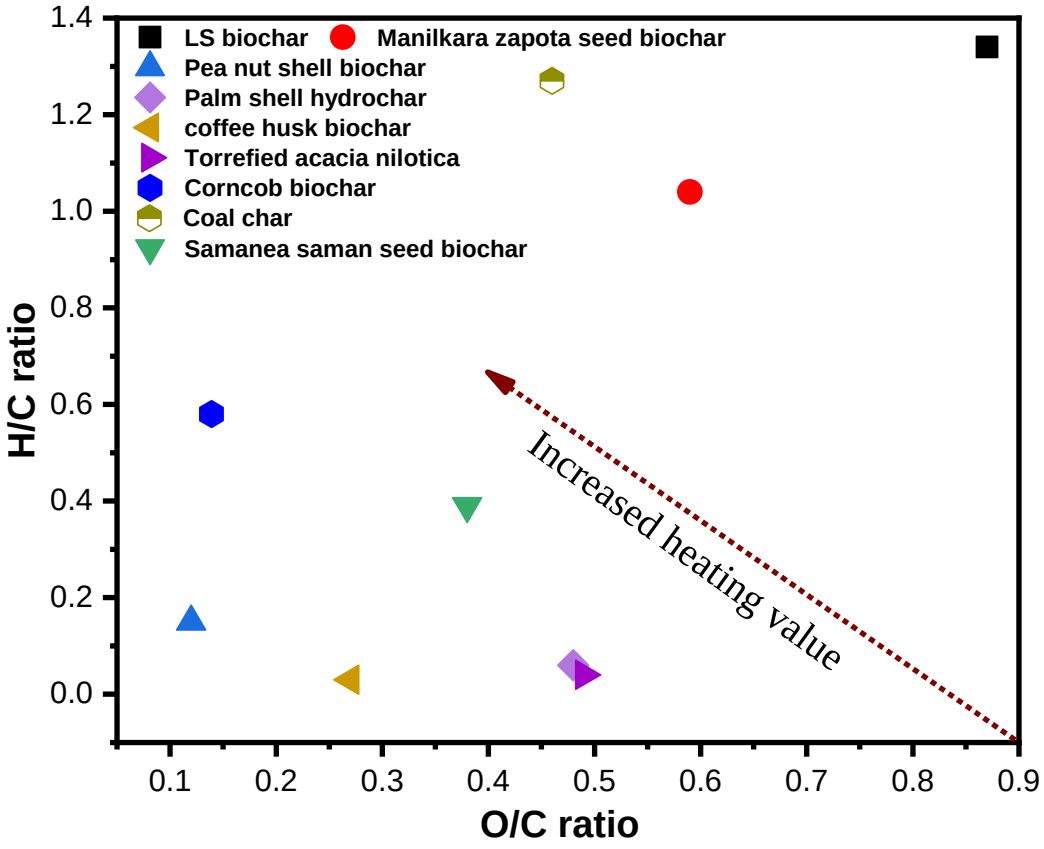


**Fig. 4.13:** Van-Krevelen diagram of LS biochar along with other reported biochar

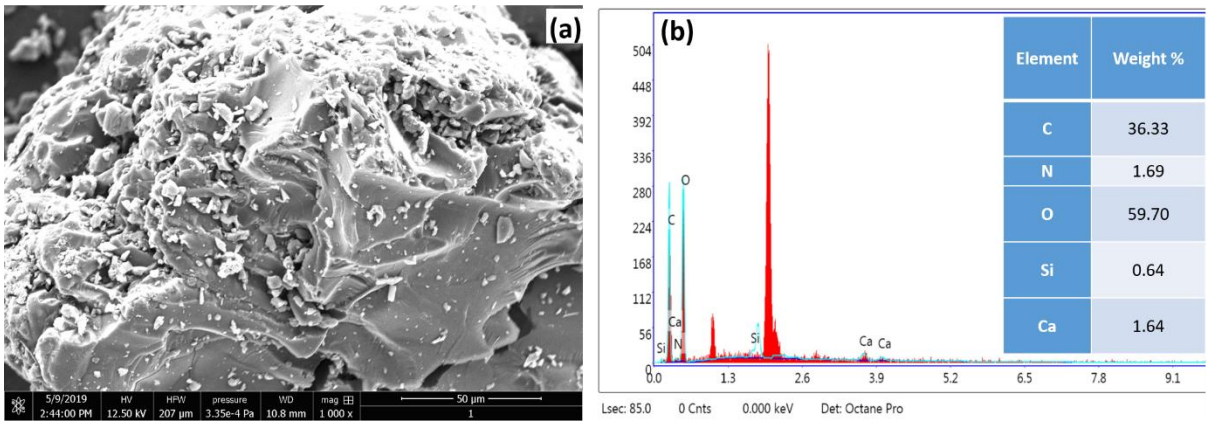


**Fig. 4.14:** (a) FE-SEM, and (b) EDX analysis of LS biochar

## 4.7 Conclusion

The pyrolysis kinetic behavior and thermal pyrolysis of LS biomass were executed in a thermogravimetric analyzer and in a fixed bed reactor, respectively. The physicochemical analysis results revealed that LS biomass has a high potential for bioenergy production. Thermal stability analysis of biomass at dynamic heating rates verified that when heating rates

increased, the degradation peak moved to a higher location without affecting the degradation pattern. The kinetic study demonstrated that the results of the pyrolysis experiment are consistent with the experimental data. The change in enthalpy, Gibbs energy, and entropy indicated the type of the reaction, energy provided by the components, and reactivity of the system, respectively. The experimental findings revealed that the optimum condition for the maximum bio-oil yield (45.6%) was: temperature = 550°C, heating rate = 65°C/min, and flow rate of inert gas ($N_2$) = 60ml/min; however, at this condition, the predicted bio-oil yield using RSM was 44.98%. ANOVA results revealed that the influence of temperature was greater than the influence of heating rate and $N_2$ flow rate, whereas the influence of $N_2$ flow rate was minimal in contrast to heating rate and temperature. The physicochemical characterization of the bio-oil revealed its acidic character, while the FTIR and 1H-NMR findings indicated the attendance of different functional groups. Physicochemical characteristics of LS biochar, such as HHV (17.77 MJ/kg), carbon content (43.45%), BET surface area (16.19 $m^2/g$), zeta potential (-32.43 mV), and bulk density (503.3 $kg/m^3$), revealed its multiple application. The relevance of these findings is that LS bio-oil may be utilized as a substitute for domestic heating purposes or for the extraction of many valuable chemicals; however, it requires further upgrading to be used as a substitute for commercial fuel. Biochar can be used for a variety of purposes such as solid fuel, fertilizer, soil additives, bio-composite, etc.